Melting and refreezing of zirconium observed using ultrafast x-ray diffraction

Harry B. Radousky [1,*] Michael R. Armstrong,[1] Ryan A. Austin,[1] Elissaios Stavrou [1] Shaughnessy Brown,[2]
Alexander A. Chernov,[1] Arianna E. Gleason,[2,3] Eduardo Granados,[2] Paulius Grivickas,[1] Nicholas Holtgrewe,[4]
Hae Ja Lee,[2] Sergey S. Lobanov,[4] Bob Nagler,[2] Inhyuk Nam,[2] Vitali Prakapenka [5] Clemens Prescher,[6] Peter Walter,[2]
Alexander F. Goncharov [4] and Jonathan L. Belof[1]

[1]*Lawrence Livermore National Laboratory, Physical and Life Sciences Directorate,*
P.O. Box 808 L-350, Livermore, California 94550, USA
[2]*SLAC National Accelerator Laboratory, Menlo Park, California 94025, USA*
[3]*Los Alamos National Laboratory, Los Alamos, New Mexico 87545, USA*
[4]*Geophysical Laboratory, Carnegie Institution of Washington, Washington DC 20015, USA*
[5]*Argonne National Laboratory, Argonne, Illinois 60439, USA*
[6]*Institute for Geology and Mineralogy, University of Cologne, Cologne 50923, Germany*

Ultrafast (130-fs) x-ray diffraction at the Linac Coherent Light Source has been applied to observe shock melting, which is driven by a rapid (120-ps) laser pulse impinging on a thin (few micrometers) bilayer of aluminum/zirconium. At a pressure of 100 GPa in the aluminum (130 GPa in the zirconium), there is rapid melting of both metals and the recrystallization of zirconium into the bcc β phase. We observe the solidification of the melt starting a few hundred picoseconds following the shock melting, out to 50 ns when the zirconium is fully crystallized into the bcc β phase at a residual temperature of approximately 2000 K. The pressure is obtained directly from the early time x-ray data, whereas the additional information from the x-ray line width and intensity at longer times inform a model of crystal nucleation and growth.

I. INTRODUCTION

Melting and freezing are one of the most common experiences [1], yet can be difficult to understand since the fundamental mechanisms occur on near-atomic and picosecond timescales [2–7]. Detailed knowledge of these mechanisms (and the ability to control them) has the potential to revolutionize how we view melting and freezing as well as applications, such as material synthesis of metallic glasses [6,7]. Since equilibration of metals upon rapid compression occurs on the timescale of the lattice vibrations, traditional long timescale (1–10-ns) compression experiments [8] cannot observe the melting transition mechanisms which are fundamentally a picosecond phenomena. More recently, several groups have looked at the melting of Al [9], Bi [10], and Sc [11] using a >10-ns laser. In particular, using a shock release method, Gorman *et al.* [10] observe melting on the timescale of 3 ns. In order to study the fundamental aspects of melting, it is necessary to use laser pulses on the picosecond timescale. These measurements are accompanied by the need to have thinner samples. In particular, for shock speeds on

the order of 5–10 nm/ps, a 100-ps duration laser drive will require a sample on the order of a few micrometers. These experiments also required the development of capabilities to analyze nonsteady shocks within the samples. In addition, velocimetry [12], which is conventionally used to estimate pressure and density of dynamically compressed samples in longer duration experiments, is not typically available at the picosecond timescale, which required the development of an ability to derive the shock pressure using the 100-fs x-ray data alone. Here, we report on results using the SLAC/Linac Coherent Light Source (LCLS) x-ray free-electron laser where zirconium was dynamically compressed to a pressure of 130 GPa, using an ∼120-ps duration laser drive (20-ps rise time) and interrogated by 130-fs duration x-ray pulses.

Dynamic compression experiments [8], typically require timescales of several nanoseconds to ensure equilibration. Our fast compression experiments conducted at the LCLS Matter in Extreme Conditions (MEC) employed uniaxial compression, which accesses far-from-equilibrium mechanical states under extreme shear stress. Conventional picosecond timescale compression experiments can, by characterizing the flow of material, determine the time-dependent bulk stress/strain state within a sample. Such experiments have been used to observe a wide range of anomalous behavior, including extreme elastic deformation, simultaneous phase transformation and plasticity, and strain-rate-dependent shock-induced chemistry [13–16]. These previous experiments did not, however, have access to femtosecond x-ray diffraction and, therefore, could not provide a direct measure
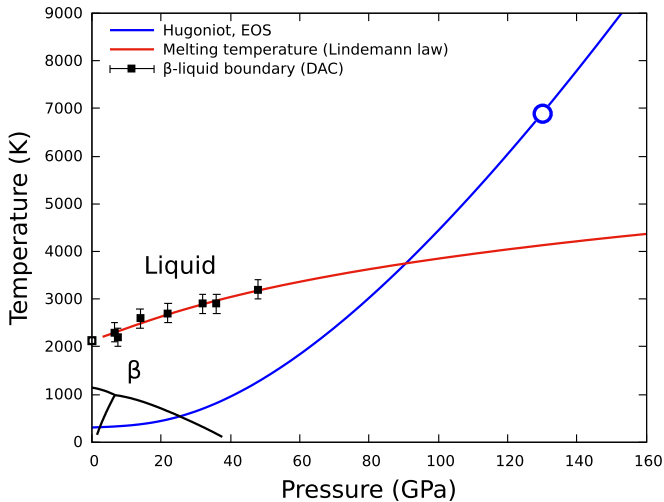
*radousky1@llnl.gov

FIG. 1. Phase diagram for Zr. Solid-solid phase lines are taken from Ref. [17]. Melt line data, calculated melt curve, and the shock Hugoniot were determined as described in the text. The blue circle indicates the location of our data point.

of the atomic structure. Zr is well suited for studying material transformations due to its complex phase diagram allowing the study of three solid-solid phase transformations [17] plus the melt transition at pressures readily attainable at the MEC instrument [9]. Our studies of compression and release at the 100-ps timescale and 130-GPa pressure reveal melting within 100 ps of shock arrival, in-line with a recent study on Bi melting [18], and refreeze starting within hundreds of picoseconds after release. In addition, we follow the refreeze to 50 ns and observe substantial refreeze into the β-Zr phase.

II. EXPERIMENTAL AND COMPUTATIONAL METHODS

The melting line of Zr, under static high-pressure conditions, was determined in this paper using a laser-heated diamond-anvil cell) with micron-spatial resolution and a well-established time-resolved approach [19,20]. Details about the loading procedure, pressure determination, and temperature measurement can be found elsewhere [21,22]. The experimental results are shown in Fig. 1 together with a Lindemann-derived melt line calculated in this paper, the Zr phase diagram and the Zr shock Hugoniot (a curve which gives thermodynamic variables for a range of final states subsequent to shock compression). Good agreement is observed between the experimentally determined and the Lindemann-derived melting lines. A recent study of the melting line of Zr under static conditions [23], using, essentially, the same method we used here gave a near-perfect agreement in the 30–50 GPa overlap range.

The Zr Hugoniot curve was calculated using an equation of state [24], which has been fit to shock compression data up to 140 GPa [25]. This equation of state (EOS) does not distinguish among the different phases of Zr that may be present along the shock compression pathway. As such, the Hugoniot temperature is overestimated because the latent heats of transformation are neglected. From previous work [17], the latent heat of the α-ω transformation is rather small, whereas the

Hugoniot temperature would be reduced by ~500 K across the ω-β boundary. As discussed later, the latent heat of melting would reduce the temperature by another ~400 K. Therefore, the Hugoniot temperature predicted at 130 GPa is too high by ~900 K but still well above the extrapolated melt line.

An Al ablation layer and Zr sample layer were sputter coated on a SiN-coated Si wafer which had been chemically etched to give a 15×15 array of 550-μm^2 SiN windows, spaced by 1 mm. X-ray photoelectron spectroscopy (XPS) with Al $K\alpha$ x rays was used for elemental compositional analysis. Each XPS measurement was obtained by an x-ray beam focused to a 200-μm spot on a probed sample surface while gradually sputtering the surface with a 3-kV Ar$^+$ ion beam. The absence of oxygen and Hf peaks in the full XPS spectra suggests that the Zr film was pure up to 0.1% in atomic mass (resolution of the XPS system). The 2.2-μm Al ablator (coated on a thin SiN window) is driven by a 250-mJ ~120-ps FWHM duration laser pulse with a 20-ps initial rise, greater than a 30-μm spot size launching a shock wave of similar duration into the ablator. The drive laser rise time is consistent with previous work [13–16]. The intensity contrast of the pulse is sufficient to avoid significant preheating >100 K from estimates of the Al Bragg peaks shifts based on the known thermal EOS of Al at ambient pressure. We do not observe any thermal shift of the Al Bragg peaks between the static x-ray diffraction (XRD) patterns, acquired without the driving laser, and the XRD patterns acquired at early times (e.g., −30 ps) before the laser drive. The shock wave transits the Al ablator and enters the 1.7-μm-thick Zr sample where rapid compression initiates a phase transition to a melted state in both the Al and in the Zr. After a variable delay, an ~100-fs duration x-ray pulse with less than a 5-μm diameter cocentered with the drive laser is used to obtain an XRD pattern from the sample, providing structural information during the compression wave transit through the sample. Using this method on a set of identical samples by varying the delay between the laser drive and the x-ray pulse, the progress of phase transformations in the Zr sample can be tracked with better than picosecond time resolution. This resulted in peak pressures of 100 GPa in the Al, corresponding to 130 GPa in the Zr, which is obtained by shock impedance matching with the Al ablator.

III. RESULTS AND DISCUSSION

Figure 2 shows the 2D x-ray images taken at −30, 600 ps, and at 50 ns, and the melting of both metals can be seen in the figure. At the initial −30 ps, one can see both the ambient pressure rings for Al plus the rings for the hexagonal Zr. At 600 ps, both metals are melted with broad diffraction seen characteristic of melted Zr. At 50 ns, the lines indicate recrystallization of the Zr into the body centered cubic (bcc) structure. The relatively broad Debye rings of Zr could be attributed to the the presence of residual stress/texturing due to the preparation method (sputtering) of the targets.

Selected one-dimensional integrated diffraction patterns are shown in Fig. 3. Subsequent to compression of Zr, solid Al peaks are seen to be reduced and then disappear, indicating that Al had melted under shock compression [26]. Based on
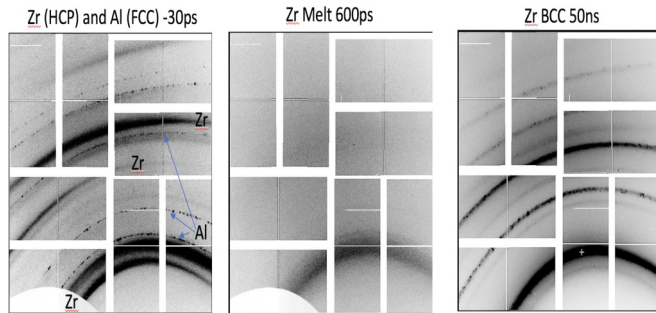
FIG. 2. X-ray diffraction two-dimensional (2D) images for $t = -30$, 600 ps, and 50 ns. At 600 ps, one observes diffraction features associated with melting of both Zr and Al, followed by the recrystallization of Zr into the bcc structure.

linear variation of the ambient Al peak intensity with time (see Fig. 4), the shock wave speed in the Al ablator for 250-mJ drive energy was estimated to be 10.2 km/s with an error of 10%, corresponding to a shock pressure (assuming the known Hugoniot of Al) of 100 GPa.

To help determine the timing of compression and release waves in the sample and the distributions of pressure, plane-wave propagation in the Al/Zr layers was simulated using a LLNL hydrodynamic simulation code. The compression wave was generated by a pressure boundary condition prescribed on the back surface of the Al layer with a peak amplitude and time variation selected to emulate the laser drive. The
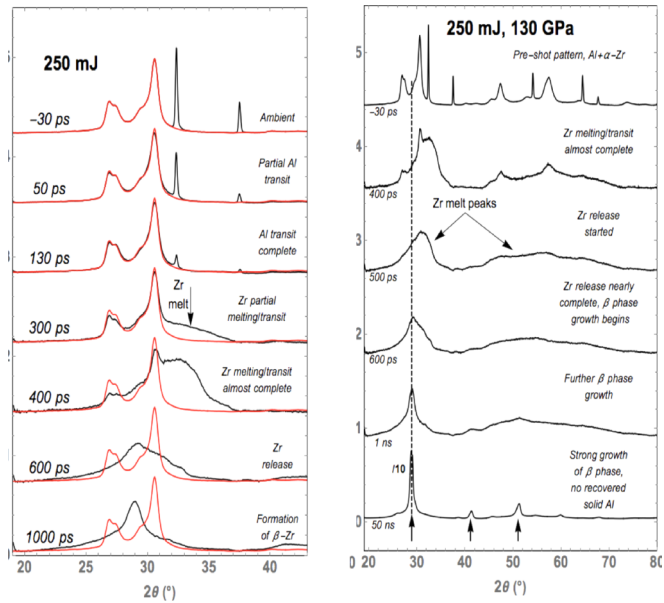

FIG. 3. X-ray diffraction as a function of increasing delay time. Each pattern represents a separate experiment on a set of identically prepared samples. The delay time varies in the left panel from before the pulse arrives (-30 ps) to 1000 ps. In the right panel, delays vary from 400 ps out to 50 ns. The zirconium is under pressure and shock melted from approximately 300–600 ps. From 600 ps out to 50 ns, recrystallization occurs. The red traces are the Zr background with Al diffraction peaks removed for comparison to time-resolved data in black. The x-ray wavelength is $\lambda = 1.301$ Å. The Bragg peaks of the β-Zr phase are noted with arrows.
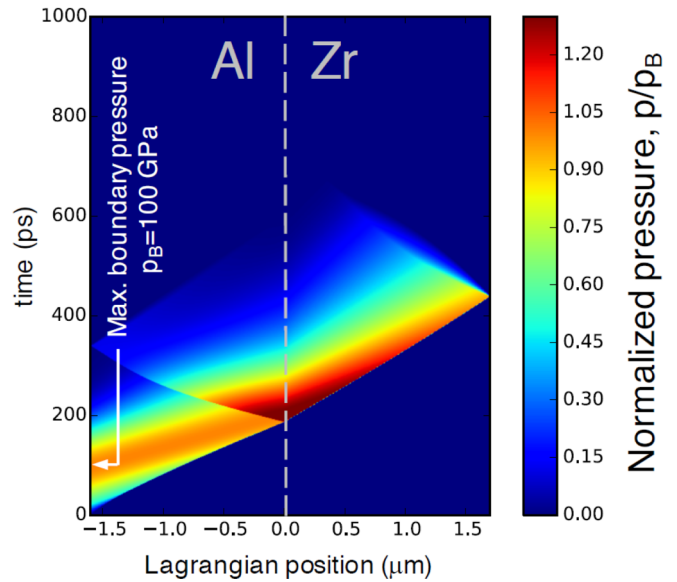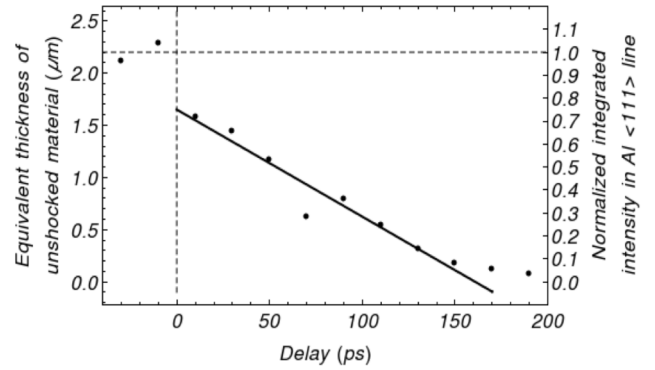

FIG. 4. The top panel shows the thickness of the unshocked Al ahead of the shock front, determined from the integrated area under the Al peaks. This gives the shock speed as 10.2 km/s. The bottom panel shows the simulated pressure field plotted on the space-time (X-t) plane, which was obtained using a hydrocode calculation.

simulated thickness of the Al layer was reduced to the experimentally observed value at zero delay time (1.6 μm) to account for ablation of material at the drive surface. The thermomechanical response of each layer (Al and Zr) is described using a Mie-Gruneisen EOS and a constant heat capacity. Deviatoric stresses are neglected, and tensile pressures are not supported. The simulations employ the adiabatic assumption with temperatures computed from the difference between the internal energy and the cold energy. The selected EOS parametrizations reproduce the shock Hugoniot data for Al and Zr [25]. Here, we note that the equations of state do not distinguish among the different solid phases of Zr, nor do they account for melting of either Al or Zr. In Fig. 4(b), the simulated pressure fields are plotted in the space of Lagrangian position (X) versus time (t). The pressure wave in Al steepens up before reflecting from the interface at 180 ps. A pressure wave with a peak amplitude of 130 GPa then travels into the Zr layer. Release waves return the pressure in the Zr layer back to zero around 600–700 ps. Hydrodynamics simulations designed to emulate the experimental conditions, also shown in Fig. 4, illustrate the progress of the compression
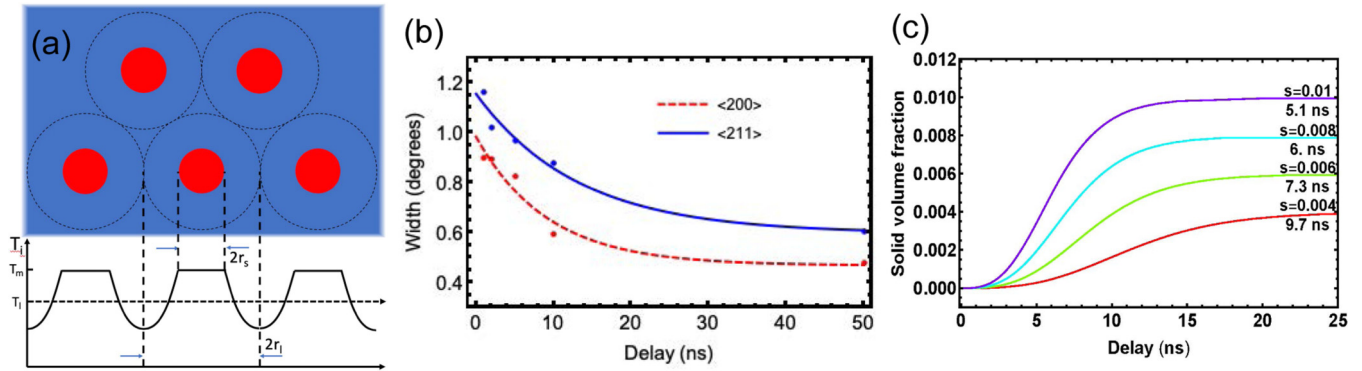
FIG. 5. (a) The pictorial model for crystal growth, with latent heat diffusing radially outward from the center of the solid nucleus and reducing the subsequent growth of neighboring crystallites. (b) The time-dependent variation of the experimental x-ray linewidths, which give a value for r_S through the Scherrer equation, obtained by fitting a Lorentzian to the measured lineshapes. Panel (c) shows the integrated solid volume fraction from the heat-coupled, time-dependent crystal growth model, Eq. (3), as a function of time, at different values of initial dimensionless supercooling $s = (T_m - T_0)/T_Q$.

wave through the Al/Zr sample as a function of time and match the observed times within the error bars. The rapid drop near $t = 0$ of the Al lines is due to laser ablation, which launches the shock wave. This results in the loss of crystalline structure of Al, see Fig. 3, over an approximately 500-nm thickness of material on the laser side of the Al ablator. The observed transit time accounts for transit through an ambient material, which is 500 nm thinner than the initial Al ablator thickness. This loss of crystallinity also provides information about ballistic electron thermal transport at very high fluence.

The remaining broad diffraction is consistent with liquid Zr. We note that the melted Al at 400 ps is released in pressure and would overlap the Zr melt peak which is still under pressure. It is expected that the majority of this broad peak derives from the Zr due to its higher scattering factor. In addition, no large Al melt peak is observed at later times once the Zr peak has shifted back to the lower angle. We also note that, at late times up to 50 ns, the Al peaks do not reappear. This implies that Al remains melted over this time period, which is consistent with its low melting temperature compared to Zr, and the high residual temperature of the Zr out to late times due to the latent heat of recrystallization.

Shock melting of Zr is evident within ~100 ps (~300-ps absolute time) after shock arrival in Zr via the appearance of broad pressure-shifted peaks consistent with a compressed liquid. Ambient Zr peaks decrease in intensity at subsequent delays as the shock transits the Zr sample. Partial release at 500 ps shifts the broad peaks to lower angles followed by nearly complete release at 600 ps and evidence of initial growth of β-Zr. Further growth of β-Zr occurs on nanosecond timescales where much stronger diffraction peaks at 50 ns likely indicate high crystallinity growth from the liquid phase.

Our sample contains less than 0.1% (atomic) of both oxygen and hafnium meaning the melt line will not be significantly shifted. We clearly observe the melting of Zr at the shock pressure corresponding to 130 GPa in the Zr. Melting at this shock pressure is consistent with crossing the melting line shown in Fig. 1. Of note is the recrystallization of the β phase, existing to late times of, at least, 50 ns. The data show a very strong diffraction signature compared to the

original α-Zr phase, which indicates a new texturing as it grows from the melt phase. From both the higher angle-shifted location of the diffraction peak and the timing, Zr is melting under compression. Also, at 50 and 130 ps, we observe a substantial decrease in the intensity of the ambient Al $\langle 111 \rangle$ peak, suggesting (along with the estimated 1-Mbar shock pressure) that the Al is shock melted on compression and stays melted upon reflection of the shock at the Al/Zr interface. The presence of broad melt peaks in both Al and Zr is consistent with the estimate of shock pressure in the Al ablator given by the shock speed from Fig. 4.

As shown in Fig. 3, the Zr melting occurs between the times of about 300 and 600 ps, thus, lasting ~300 ps. Crystallization begins ~200 ps after melting and crystallization was followed out to a very long time of 50 ns. Our simulation of the shock wave propagation through the sample, Fig. 4 (the right panel), shows that the pressure in the sample releases to zero pressure at about 600–700 ps. This is compared to the time for crystallization which is observed out to 50 ns. This quick cooling followed by a long crystallization time is analogous to the temperature time plateau observed by calorimetry in conventional crystallization at ambient conditions. This plateau comes from the latent heat and is self-consistently maintained since the external cooling is compensated by the heat generated during crystallization in the melt-crystal slurry.

The average crystallite size at time t follows from the β-Zr crystal diffraction linewidths $w(t)$, whereas the ratio of the diffraction intensity at a given moment of time to the maximal intensity reached at 50 ns can be used as a measure of the solidified part in the sample by that time under the assumption that by 50 ns the solidification is substantially complete. The data are shown in Fig. 5.

The Scherrer equation provides the average radius of crystallites $r_s(t)$,

$$r_s(t) = \frac{K\lambda}{[w(t) - w_{\text{in}}]\cos\theta}. \quad (1)$$

Here, w is the width of the diffraction line at its half maximum in radians at the diffraction angle θ whereas $w_{\text{in}}(= 0.1°)$ is the instrumental linewidth. The radiation

wavelength is $\lambda = 1.3$ Å. For the spherical crystallites, the constant $K = 1.11$. Equation (1) for $t = 1$ ns results in crystal radii $r_S = 7.6$, 5.5, and 4.3×10^{-7} cm for the lines diffracting at $\theta = 14.4°$, $20.65°$, and $25.5°$, respectively. At $t \leqslant 10$ ns, the diffraction intensity shows that the solid fraction $\phi \ll 1$. Therefore, we assume that each crystal sphere sits in the center of a concentric liquid cell with radius $r_L = \phi^{-1/3} r_s$ remaining constant in time. The cells form a lattice [Fig. 5(a)] and are taken to be equal, making each thermally isolated. Comparing the crystal radii at $t = 1$ and 2 ns, one may estimate the average growth rate to be $V \approx 150$ cm/s. At the later times, the growth rate decreases.

The growth rate of 150 cm/s estimated above allows an estimate of the average supercooling in the slurry. Since the zirconium entropy of fusion is low [27–29], $\Delta S = 1.04k$ (where k is the Boltzmann constant), the crystal-melt interface is assumed to be disordered. Therefore, the growth rate V is given by Eq. (2) and is proportional to the crystallization driving force $\Delta \mu / kT_i$ where $\Delta \mu$ is the difference between the liquid and the solid chemical potentials. T_m is the melting temperature at ambient pressure and T_i is the temperature at the interface [30,31]

$$V = \frac{\beta \Delta \mu}{kT_i} \equiv \beta_T (T_m - T_i). \qquad (2)$$

In the numerical estimates below, we distinguish the interface temperature T_i from the bulk melt temperature T only when it enters the interface supercooling and is multiplied by the large kinetic coefficient $\beta = \left(\frac{kT_i}{m}\right)^{1/2} = 4 \times 10^4$ cm/s determining the growth rate [31] $\beta_T = 19$ cm/s K.

Using the cell model, the cooling process may be separated into two parts. The first is adiabatic cooling due to the release of pressure in a thermally isolated cell. Its initial temperature may be T_m if crystal seeds are present or is much lower, down to $0.7T_m$ if homogeneous nucleation is possible [32,33]. The seeded or nucleated crystals grow until the supercooling falls to zero. This supercooling depends on the initial temperature, total adiabatic temperature drop, and on the latent heating temperature $T_Q = T_m \Delta S / c_P$, the ratio of the latent heat to the heat capacity. For Zr, we take the temperature rise due to latent heat to be $T_Q = 423$ K based on previously measured values at ambient conditions [34]. This is the temperature rise in a melt of elemental Zr crystallized under thermally and mechanically isolated conditions. Unless the initial temperature is deep below the melting point, the final cell temperature reaches the melting point before the whole melt is crystallized. That low undercooling case is probably realized in these experiments and the second part of the cooling begins. This part is controlled by the latent heat transport out of the whole sample rather than the small cell. Therefore, that second part may last much longer.

A crystallite of a nanoscale radius $r_S \approx 10^{-6}$ cm or smaller growing in a supercooled melt is expected to be heated close to the melting point within the time of $\sim (r_S^2)/4\alpha \approx 2$ ps where the Zr thermal diffusivity $\alpha \approx 0.12$ (cm)^2/s [35]. Later, the growing crystal has nearly no ability to absorb more latent heat so that all latent heat goes to the melt. During the initial adiabatic part of the process, the average liquid temperature $\overline{T_l}$ is controlled by the simplified heat balance equation within the cell, coupled with the crystal growth

rate $\frac{dr_s}{dt}$ and with a driving force supplied by the rate of undercooling, $g(t)$:

$$\frac{d\overline{T_l}}{dt} = \frac{3T_Q r_S^2}{r_l^3 - r_S^3} \frac{dr_S}{dt} - g(t),$$

$$\frac{d}{dt}\left(\frac{r_S}{r_l}\right) = \frac{\beta_T}{r_l}(T_m - T_i) \approx \frac{\beta_T}{r_l}(T_m - \overline{T_l})$$

$$= \frac{1}{\tau}\left\{\frac{T_m - T_0}{T_Q} + \ln\left[1 - \left(\frac{r_S}{r_l}\right)^3\right]\right\}. \qquad (3)$$

The second line of Eq. (3) follows from Eq. (2) where the crystal interface temperature $T_i(t)$ is approximated by the integral $\overline{T_l}(t)$ obtained from the first line of Eq. (3). The integration constant T_0 is the melt temperature at $t = 0$ plus the integral of $g(t)$ over $t > 0$, both unknown. The solution of the second line of Eq. (3) is presented in Fig. 5(c) for several initial constant values of the supercooling $s = (T_m - T_0)/T_Q$. The characteristic timescale for the process $\tau \equiv r_L/\beta_T T_Q = 300$ ps where the numerical estimate is for the experimental $r_L \cong 2.4 \times 10^{-6}$ cm. Cessation of the fast growth at 6 ns suggests the transition to latent heat being transported over the whole sample rather than the small cell. Further sample cooling due to radiation may require microseconds to occur, which is beyond the timescale of relevance to this system.

We observed melting of metals on the timescale of a few hundred picoseconds, and we observed the recrystallization of Zr on timescales up to 50 ns. The shock speed in Al was determined entirely from the x-ray diffraction patterns, allowing us to determine the pressure in Zr from impedance matching. The latent heat of crystallization is found to provide the energy for the recrystallization process to extend out to 50 ns following a 120-ps pulse which drove the initial shock melting. The fact that we observe refreeze rather than a metallic glass indicates that the formation of single phase metallic glasses, even with these extremely high cooling rates, may be fundamentally limited.

[1] M. A. Sánchez, T. Kling, T. Ishiyama, M.-J. v. Zadel, P. J. Bisson, M. Mezger, M. N. Jochum, J. D. Cyran, W. J. Smit, H. J. Bakker, M. J. Shultz, A. Morita, D. Donadio, Y. Nagata, M. Bonn, and E. H. G. Backus, Proc. Natl. Acad. Sci. USA **114**, 227 (2017).

[2] V. I. Levitas and R. Ravelo, Proc. Natl. Acad. Sci. USA **109**, 13204 (2012).

[3] E. K. Cerreta, G. T. Gray, C. P. Trujillo, D. W. Brown, C. N. Tomé, M. Elert, M. D. Furnish, R. Chau, N. Holmes, and J. Nguyen, in *Proceedings of the Conference of the American Physical Society Topical Group on Shock Compression of Condensed Matter*, edited by M. Elert, M. D. Furnish, R. Chau, N. Hollmes, and J. Nguyen, AIP Conf. Proc. No. 955 (AIP, New York, 2007), p. 635.

[4] J. Zhang, Y. Zhao, C. Pantea, J. Qian, L. L. Daemen, P. A. Rigg, R. S. Hixson, C. W. Greeff, G. T. Gray III, Y. Yang, L. Wang, Y. Wang, and T. Uchida, J. Phys. Chem. Solids **66**, 1213 (2005).

[5] M. T. Pérez-Prado and A. P. Zhilyaev, Phys. Rev. Lett. **102**, 175504 (2009).

[6] Y. Ju, Q. Zhang, Z. Gong, G. Ji, and L. Zhou, J. Appl. Phys. **114**, 093507 (2013).

[7] J. Zhang and Y. Zhao, Nature (London) **430**, 332 (2004).

[8] W. Nellis, *Ultracondensed Matter by Dynamic Compression* (Cambridge University Press, Cambridge, UK, 2017).

[9] L. B. Fletcher, H. J. Lee, T. Döppner, E. Galtier, B. Nagler, P. Heimann, C. Fortmann, S. LePape, T. Ma, M. Millot, A. Pak, D. Turnbull, D. A. Chapman, D. O. Gericke, J. Vorberger, T. White, G. Gregori, M. Wei, B. Barbrel, R. W. Falcone, C.-C. Kao, H. Nuhn, J. Welch, U. Zastrau, P. Neumayer, J. B. Hastings, and S. H. Glenzer, Nat. Photon. **9**, 274 (2015).

[10] M. G. Gorman, R. Briggs, E. E. McBride, A. Higginbotham, B. Arnold, J. H. Eggert, D. E. Fratanduono, E. Galtier, A. E. Lazicki, H. J. Lee, H. P. Liermann, B. Nagler, A. Rothkirch, R. F. Smith, D. C. Swift, G. W. Collins, J. S. Wark, and M. I. McMahon, Phys. Rev. Lett. **115**, 095701 (2015).

[11] R. Briggs, M. G. Gorman, A. L. Coleman, R. S. McWilliams, E. E. McBride, D. McGonegle, J. S. Wark, L. Peacock, S. Rothman, S. G. Macleod, C. A. Bolme, A. E. Gleason, G. W. Collins, J. H. Eggert, D. E. Fratanduono, R. F. Smith, E. Galtier, E. Granados, H. J. Lee, B. Nagler, I. Nam, Z. Xing, and M. I. McMahon, Phys. Rev. Lett. **118**, 025501 (2017).

[12] S. B. Brown, A. Hashim, A. Gleason, E. Galtier, I. Nam, Z. Xing, A. Fry, A. MacKinnon, B. Nagler, E. Granados, and H. J. Lee, Rev. Sci. Instrum. **88**, 105113 (2017).

[13] J. C. Crowhurst, M. R. Armstrong, K. B. Knight, J. M. Zaug, and E. M. Behymer, Phys. Rev. Lett. **107**, 144302 (2011).

[14] M. R. Armstrong, J. M. Zaug, N. Goldman, I.-F. W. Kuo, J. C. Crowhurst, W. M. Howard, J. A. Carter, M. Kashgarian, J. M. Chesser, T. W. Barbee Jr., and S. Bastea, J. Phys. Chem. A **117**, 13051 (2013).

[15] J. C. Crowhurst, B. W. Reed, M. R. Armstrong, H. B. Radousky, J. A. Carter, D. C. Swift, J. M. Zaug, R. W. Minich, N. E. Teslich, and M. Kumar, J. Appl. Phys. **115**, 113506 (2014).

[16] M. R. Armstrong, P. V. Grivickas, A. M. Sawvel, J. P. Lewicki, J. C. Crowhurst, J. M. Zaug, H. B. Radousky, E. Stavrou, C. T. Alviso, J. Hamilton, and R. S. Maxwell, J. Polym. Sci. Part B: Polym. Phys. **56**, 827 (2018).

[17] C. W. Greeff, Modell. Simul. Mater. Sci. Eng. **13**, 1015 (2005).

[18] C. M. Pépin, A. Sollier, A. Marizy, F. Occelli, M. Sander, R. Torchio, and P. Loubeyre, Phys. Rev. B **100**, 060101(R) (2019).

[19] S. Anzellini, A. Dewaele, M. Mezouar, P. Loubeyre, and G. Morard, Science **340**, 464 (2013).

[20] A. Dewaele, M. Mezouar, N. Guignot, and P. Loubeyre, Phys. Rev. Lett. **104**, 255701 (2010).

[21] E. Stavrou, L. H. Yang, P. Söderlind, D. Aberg, H. B. Radousky, M. R. Armstrong, J. L. Belof, M. Kunz, E. Greenberg, V. B. Prakapenka, and D. A. Young, Phys. Rev. B **98**, 220101(R) (2018).

[22] V. B. Prakapenka, A. Kubo, A. Kuznetsov, A. Laskin, O. Shkurikhin, P. Dera, M. L. Rivers, and S. R. Sutton, High Pressure Res. **28**, 225 (2008).

[23] P. Parisiades, F. Cova, and G. Garbarino, Phys. Rev. B **100**, 054102 (2019).

[24] D. J. Steinberg, *Equation of State and Strength Properties of Selected Materials*, Lawrence Livermore National Laboratory Technical Report No. UCRL-MA-106439, 1996 (unpublished).

[25] S. P. Marsh, *LASL Shock Hugoniot Data* (University of California Press, Berkeley, CA, 1980).

[26] J. A. Moriarty, D. A. Young, and M. Ross, Phys. Rev. B **30**, 578 (1984).

[27] V. N. Korobenko and A. I. Savvatimskii, High Temp. **39**, 659 (2001).

[28] V. N. Korobenko and A. I. Savvatimskii, High Temp. **39**, 525 (2001).

[29] V. N. Korobenko and A. I. Savvatimskii, High Temp. **39**, 485 (2001).

[30] A. A. Chernov, *Modern Crystallography III. Crystal Growth*, Pt I. Springer Solid State Sci. Vol. 36 (Springer, Berlin, 1984).

[31] L. Mikheev and A. Chernov, J. Cryst. Growth **112**, 591 (1991).

[32] P. C. Myint, A. A. Chernov, B. Sadigh, L. X. Benedict, B. M. Hall, S. Hamel, and J. L. Belof, Phys. Rev. Lett. **121**, 155701 (2018).

[33] P. C. Myint and J. L. Belof, J. Phys.: Condens. Matter **30**, 233002 (2018).

[34] J. J. Valencia and P. N. Quested, in *ASM Handbook* (ASM International, Cleveland, OH, 2008), Vol. 15, pp. 468–481.

[35] J. Fink and L. Leibowitz, J. Nucl. Mater. **226**, 44 (1995).